# ShallowLandslider: a physics-based component for predicting regional distributions of coseismic landslides

Ghoshal, S.*[,1], Boulton, S. J.[1], Hales, T. C.[2], Bennett, G. E.[3], Beswick, A.[1], Jones, J. N.[4], Lewin, S.[1], Mildon, Z. K.[1], Stokes, M.[1], Whitworth, M. R. Z.[4], Campforts, B.[5]

[1] School of Geography, Earth and Environmental Sciences, University of Plymouth, Plymouth, United Kingdom
[2] Earth Sciences, Cardiff University, Cardiff, United Kingdom
[3] Geography, University of Exeter, Exeter, United Kingdom
[4] AECOM, United Kingdom
[5] Earth Sciences, Vrije Universiteit Amsterdam, Amsterdam, The Netherlands



Compiled on December 6, 2025

# ShallowLandslider: a physics-based component for predicting regional distributions of coseismic landslides

Ghoshal, S.*[,1], Boulton, S. J.[1], Hales, T. C.[2], Bennett, G. E.[3], Beswick, A.[1], Jones, J. N.[4], Lewin, S.[1], Mildon, Z. K.[1], Stokes, M.[1], Whitworth, M. R. Z.[4], Campforts, B.[5]

## Abstract

Earthquakes can trigger thousands of shallow landslides across mountainous terrain, reshaping landscapes and posing severe hazards. Predicting their spatial distribution remains challenging because most existing models are empirical, event-specific, and lack physical interpretability. We introduce ShallowLandslider, a physics-based component within the open-source Landlab framework for regional coseismic landslide prediction. The model extends the classical Newmark sliding block approach to three dimensions, incorporating transient seismic accelerations, slope geometry, and variable soil properties on structured grids. Instability is assessed using critical acceleration thresholds, and a probabilistic selection scheme represents natural variability in failure occurrence. We validate ShallowLandslider against landslide inventories from two subregions affected by the 2015 Mw 7.8 Gorkha earthquake in Nepal. Model performance is evaluated using non-parametric distributional metrics (Kolmogorov–Smirnov, Kuiper, and Wasserstein distances) across landslide area, elevation, slope, and aspect. Results show that realistic soil-depth parameterisations and moderate cohesion values (10 – 15 kPa) are essential for reproducing observed topographic clustering and size distributions. While pixel-level prediction remains impractical, ShallowLandslider captures first-order spatial and statistical patterns of coseismic landsliding, offering a reproducible, physically grounded tool for regional hazard assessment. Its modular design enables coupling with other Earth-surface process models, providing a foundation for integrated simulations of landscape response to seismic forcing.

## 1 Introduction

Major earthquakes can mobilise vast volumes of soil and rock from across mountainous landscapes in a matter of minutes, triggering thousands of landslides across hundreds of square kilometres. These cascading hazards often cause casualties and economic losses that can rival or even exceed those from the earthquake itself (Fan et al., 2019; Petley, 2012). Beyond their immediate human toll, earthquake-induced landslides exert a first-order control on mountain evolution, abruptly reworking drainage networks, altering valley morphology, and redistributing sediment from hillslopes to valley floors (Hovius et al., 2011; Wang et al., 2020). Understanding the physical controls on where these failures occur is therefore critical not only for hazard assessment, but also for deciphering the feedbacks between tectonics, climate, and surface processes.

Over the past several decades, various approaches have been developed to forecast the spatial distribution of earthquake-triggered landslides. Empirical susceptibility models use observed associations between landslide occurrence and terrain parameters such as slope angle, aspect, lithology, and distance to faults (e.g., Kritikos

[1] *School of Geography, Earth and Environmental Sciences, University of Plymouth, Plymouth, United Kingdom*
[2] *Earth Sciences, Cardiff University, Cardiff, United Kingdom*
[3] *Geography, University of Exeter, Exeter, United Kingdom*
[4] *AECOM, United Kingdom*
[5] *Earth Sciences, Vrije Universiteit Amsterdam, Amsterdam, The Netherlands*

et al., 2015; Parker et al., 2015). While these statistical approaches are computationally efficient and perform well when trained on high-quality inventories, they are inherently event-specific, reflecting the characteristics of the earthquake and terrain from which they were derived. As a result, their transferability to new regions or earthquakes with different ground motion patterns can be limited (Gariano and Guzzetti, 2016; Tanyaş et al., 2017). More recently, machine learning and ensemble-based models have sought to overcome these limitations by capturing complex, non-linear relationships between multiple conditioning factors (Reichenbach et al., 2018). While these data-driven approaches have markedly improved predictive performance, particularly when large, spatially consistent datasets are available, they remain largely empirical and often suffer from overfitting and limited physical interpretability. Recent reviews highlight that most models provide limited physical insight into the underlying physical failure mechanisms or the role of key controlling parameters such as soil thickness and strength, and ground motion directionality, and still depend heavily on training data quality (Lombardo et al., 2020; Nowicki Jessee et al., 2018; Reichenbach et al., 2018).

Physics-based models, in contrast, explicitly represent the mechanical processes governing slope failure and are therefore better suited for hypothesis testing and extrapolation across diverse geomorphic and seismic settings. Among these, the Newmark sliding block method remains the most widely used for assessing coseismic slope stability. The method conceptualizes a potential landslide as a rigid block resting on an inclined plane, which begins to slide once the driving acceleration exceeds a critical threshold determined by slope geometry and material strength (Jibson et al., 2000; Jibson, 2007; Newmark, 1965; Romeo, 2000). This simple and robust formulation allows implementation at various scales, particularly when combined with digital elevation models and spatially distributed ground motion data. As such, it has been widely applied to simulate coseismic landslides, particularly where rapid, shallow failures dominate the landscape response. Early studies used the method for both single failures and regional failure events, using empirical or synthetic ground motion inputs to estimate the spatial extent and cumulative displacements of potential sliding (Jibson, 2007; Keefer, 1984). However, these implementations retain the one-dimensional assumption, limiting their ability to represent the complex, three-dimensional nature of real failures (Huang et al., 2020; Ingles et al., 2006; Tsai and Lin, 2018). They are also unable to take into account the effects of topographic amplification, where steep slopes, convex ridges, and irregular terrain can locally increase ground acceleration (Dahal et al., 2024; Meunier et al., 2008). Furthermore, a persistent challenge in physics-based landslide modelling is the parameterization of material and hydrologic properties at the landscape scale, where soil depth, cohesion, and friction angle are rarely well constrained, and the resolution of available topographic data limits how small and shallow failures can be realistically represented (Segoni et al., 2012). As a result, regional models often rely on generalized assumptions that obscure local variability and complicate quantitative validation against observed landslide inventories.

Recent advances in high-resolution topography, open-access seismic data, and modular modelling frameworks now make it possible to revisit these challenges with greater realism and reproducibility. Integrating physically based slope stability theory with modern computational tools offers a pathway toward models that retain physical interpretability while being flexible enough to capture spatial heterogeneity and process coupling at the landscape scale. To address these challenges, we present *ShallowLandslider*, a new physics-based modelling component built on the Landlab framework (Barnhart et al., 2020; Hobley et al., 2017). In it, we extend the Newmark method to three dimensions based on the approach of Huang et al. (2020), enabling spatially distributed seismic inputs and variable material properties. *ShallowLandslider* is designed for reproducibility and modularity, allowing users to systematically explore how elevation, slope, aspect, soil depth, and shaking intensity influence the distribution of coseismic slope failures. The component is fully open-source and written in Python, leveraging Landlab's grid-based architecture to ensure computational efficiency and seamless coupling with other Earth-surface process models. The existing *LandslideProbability* component provides probabilistic assessments of shallow landslide initiation driven by hydrologic forcing using an infinite-slope formulation and Monte Carlo sampling (Strauch et al., 2018). However, its focus lies in rainfall- or groundwater-induced failures and parameter uncertainty rather than dynamic ground shaking. *ShallowLandslider* extends this capability by explicitly incorporating

seismic accelerations and rigid-block mechanics, allowing users to explore the spatial distribution of earthquake-triggered failures within the same modelling environment. It also complements the existing *BedrockLandslider* component, which, as its name suggests, simulates deeper-seated, bedrock-dominated failures (Campforts et al., 2020, 2022). This combination of components extends Landlab's capacity to represent a continuum of slope failure processes. By combining transparent physics with a flexible, community-oriented computational framework, *ShallowLandslider* aims to bridge the gap between detailed slope stability mechanics and regional-scale hazard assessment, providing a reproducible foundation for investigating the feedbacks between seismic forcing, topography, and landscape evolution.

## 1.1 The Gorkha Earthquake and coseismic landslides

We evaluate *ShallowLandslider* against the coseismic landslides triggered by the $M_w$ 7.8 Gorkha earthquake. The earthquake struck central Nepal on $25^{th}$ April 2015, rupturing a ~150 km segment of the Main Himalayan thrust between the Gorkha region northwest of Kathmandu to the Ramechhap region in eastern-central Nepal (Avouac et al., 2015; USGS, 2015). The earthquake produced peak ground accelerations (PGA) locally exceeding $0.6g$, and caused widespread slope failures across an area of more than $30\,000\,km^2$. Over 25000 landslides were mapped in its aftermath by a succession of groups around the world (Kargel et al., 2015; Meena and Tavakkoli Piralilou, 2019; Roback et al., 2018), making it one of the most comprehensively documented cases of coseismic landsliding worldwide. Failures were concentrated in areas of high PGA and rugged topography north of the Kathmandu valley, with smaller and fewer events occurring in the foothills to the south (Roback et al., 2018). The spatial pattern of landsliding closely followed gradients in shaking intensity and local relief, offering an ideal natural experiment for evaluating model performance in real-world conditions.

To examine the robustness of our model predictions, across spatial and seismic gradients, we have selected two subregions within the rupture zone for validation (Figure 1). Each subregion represents distinct combinations of terrain, seismicity and failures, allowing us to comprehensively test how the model performs under varying conditions.

1. Subregion 1 (northwest of Kathmandu): This subregion is located immediately to the east of the earthquake epicentre. It experienced some of the strongest shaking, with PGA ≈ 0.6g, but produced a moderate number of landslides ($n = 523$). The region is located in the headwaters of the Budhi Gandaki river and exhibits a large range in elevations, between 1500 m–6000 m (mean≈ 3800), with slopes varying almost normally between subhorizontal to extremely steep (68°), with a mean of 37°. The coseismic landslides in this subregion were concentrated at the lower end of the regional elevation distribution, with very few failures above 4000 m. More understandably, failures are largely concentrated at higher slopes, with most occurring on slopes $> 35° - 50°$ (Figure 1).

2. Subregion 2 (northeast of Kathmandu): This subregion is located northeast of Kathmandu, along the Araniko Highway toward the Nepal-China border. It is an extremely landslide-prone area, with monsoon-triggered landslides often blocking the highway. It was devastated by the earthquake, being affected by both the initial earthquake, and the aftershock in May, with PGA ≈ 0.6g, triggering over 2300 landslides. However, the average elevation in the area is considerably lower than subregion 1, ranging from 1000 m–3500 m, with a mean of approximately 2500 m. This narrow range in elevations means that landslides occur over the entire range. The slope distribution is similar to subregion 1, ranging between subhorizontal to extremely steep (≈ 60°), but with a lower mean (26°). As expected, landslides generally occur on steeper slopes ($> 35° - 50°$) (Figure 1).

Together, these subregions encompass the primary geomorphic gradients within the 2015 rupture zone and provide a robust basis for evaluating model transferability across diverse landscapes under similar seismic conditions. By comparing simulated critical accelerations and predicted landslide distributions against mapped inventories, we

evaluate whether a physically-based, three-dimensional Newmark framework can reproduce observed spatial patterns of coseismic landsliding using only topographic and seismic inputs. This case study further allows us to quantify how variability in terrain, material properties, and shaking intensity influences regional patterns of slope failure, and to assess the viability of physically-based approaches to predict landslide hazard.

# 2 Methods

Table 1: Notation and symbols used in *ShallowLandslider*

| Symbol | Description | Default Value (if any) |
|---|---|---|
| *Geometric Parameters* | | |
| $\alpha$ | Slope angle (°) | – |
| $h_s$ | Soil thickness in normal direction (m) | – |
| $m$ | Proportion of submerged soil | 0.5 |
| *Strength Parameters* | | |
| $c'$ | Effective cohesion (Pa) | – |
| $\phi'$ | Effective angle of friction (°) | 30 |
| $\phi^b$ | Angle of increase in shear strength with matric suction (°) | – |
| $FS$ | Static factor of safety | 1.0 |
| *Unit Weight* | | |
| $\gamma_t$ | Unit weight of soil ($\mathrm{kN\,m^{-3}}$) | 15 |
| $\gamma_w$ | Unit weight of water ($\mathrm{kN\,m^{-3}}$) | 9.81 |
| *Stress and Pore Pressure* (Pa) | | |
| $\sigma_n$ | Total normal stress | – |
| $\sigma_n - u_a$ | Net normal stress on the slip surface | – |
| $u_a$ | Pore air pressure | 0 |
| $u_w$ | Pore water pressure | – |
| $\psi$ | Matric suction ($u_a - u_w$) | – |
| $u$ | Pore pressure replacement for $\psi$ ($m\gamma_w h$) | – |
| *Seismic Parameters* ($\mathrm{m\,s^{-2}}$) | | |
| $g$ | Acceleration due to gravity | 9.81 |
| $a_c$ | Critical acceleration | – |
| $a_{c,transient}$ | Critical transient acceleration | – |
| $a_s$ | Sliding acceleration | – |
| $a_n$ | Acceleration normal to the slope | – |
| $a_h$, $a_v$ | Horizontal/vertical acceleration (PGA) | – |

## 2.1 Overview of the Newmark method

*ShallowLandslider* implements a modified Newmark sliding block model to identify potential areas of coseismic slope failure based on a method proposed by Huang et al. (2020). The original Newmark model is extremely useful for this type of regional analysis, particularly due to its computational and numerical simplicity. It requires very few input requirements (e.g., slope, cohesion, angle of internal friction, unit weight of soil, etc.) but is restricted to one dimension. The method implemented here extends the classical formulation to incorporate transient three-dimensional accelerations (Huang et al., 2020). In its basic form, the Newmark method conceptualises landslide initiation as the downslope displacement of a rigid block sliding on an infinite slope, driven by seismic accelerations that overcome the slope's shear resistance (Figure 2) (Jibson et al., 2000; Newmark, 1965). The onset of slope failure is determined by comparing the seismic driving acceleration with a critical acceleration ($a_c$), which represents the minimum ground acceleration required to overcome the resisting forces of the slope material (Jibson et al., 2000; Newmark, 1965). If the seismic acceleration exceeds $a_c$, the block accumulates permanent displacement and is considered unstable. The critical acceleration ($a_c$) is a function of the static factor of safety

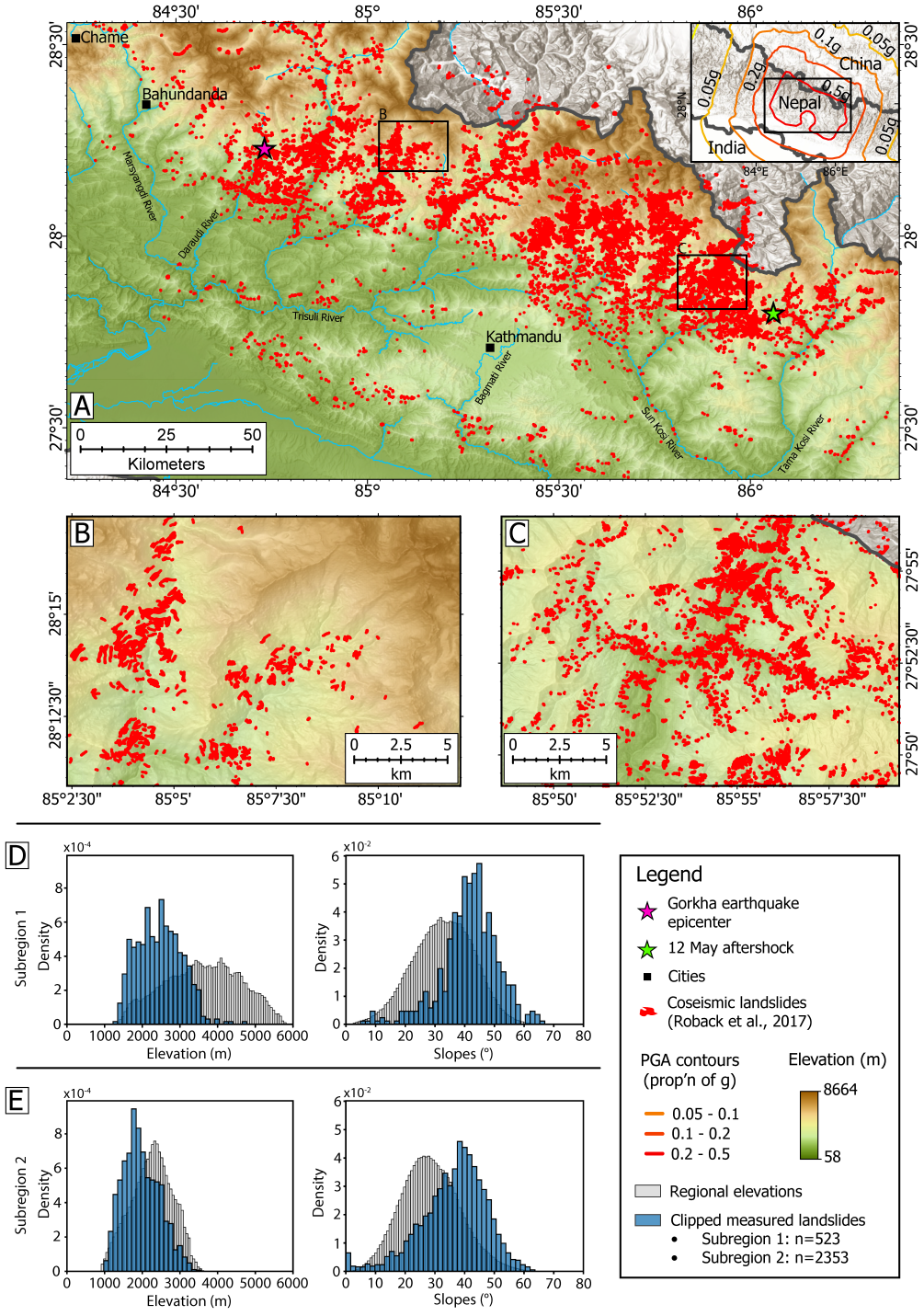


Figure 1: (A) Map showing locations of coseismic (red) landslides in central Nepal. The pink star shows the Gorkha earthquake epicentre, with the green star representing the major aftershock on 12 May 2015. The Peak Ground Acceleration produced by the earthquake are shown as contours (proportion of 'g') in the inset map, based on the USGS ShakeMap. (B) Map showing the topography and observed landslides for subregion 1. (C) Map showing the topography and observed landslides for subregion 2. (D) Histograms showing the density distributions for elevation and slope in Subregion 1. (E) Histograms showing the density distributions for elevation and slope in Subregion 2. Grey bars show regional distribution, while blue bars show distribution for mapped subregional landslides.

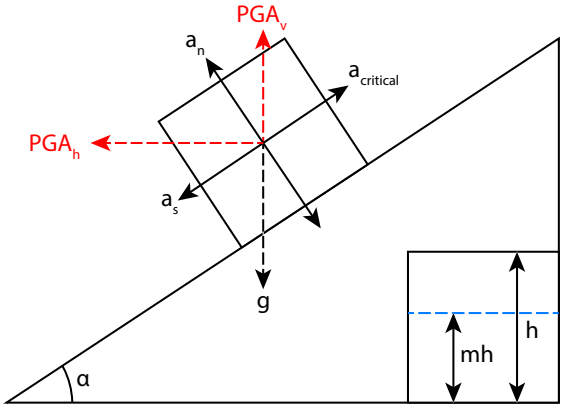


Figure 2: Box diagram showing the fundamentals of the Newmark method. The inner box depicts how the soil depth and proportion of saturation are measured in the model.

($FS$) and the slope ($\alpha$):

$$a_c = (FS - 1) * g \sin\alpha \tag{1}$$

The static factor of safety (FS) is based on the infinite slope stability model, where failure occurs along a planar surface beneath a uniform soil layer. Under saturated conditions, i.e., where the slip surface lies below the water table, the factor of safety is given by (Jibson et al., 2000):

$$FS = \frac{c'}{\gamma_t h_s \sin\alpha} + \frac{\tan\phi'}{\tan\alpha} - \frac{m\gamma_w \tan\phi'}{\gamma_t \tan\alpha} \tag{2}$$

where, $c'$ = effective cohesion, $\phi'$ = effective angle of friction, $\alpha$ = slope angle, $\gamma_t$ = unit weight of soil, $\gamma_w$ = unit weight of water, $h_s$ = thickness of sliding block in normal direction, $m$ = proportion of submerged soil.

In equation (2), the first term captures the cohesive strength, the second term represents the frictional resistance, and the third term accounts for pore water pressure effects. Slopes with $FS < 1$ are considered unstable under static conditions, with unstable slopes having $0 < FS < 1$.

In arid environments where the sliding surfaces are dry, $m = 0$, causing the third term to drop out. Since matric suction increases shear resistance along the dry slip surface, the static factor of safety becomes: (Cho and Lee, 2002; Huang et al., 2020)

$$FS = \frac{c' + (\sigma_n - u_a)\tan\phi' + (u_a - u_w)\tan\phi^b}{\gamma_t h_s \sin\alpha} \tag{3}$$

where, $u_a$ = pore air pressure, $u_w$ = pore water pressure, $u_a - u_w$ = matric suction, $\sigma_n$ = total normal stress, $\sigma_n - u_a$ = net normal stress on the slip surface, $\phi^b$ = angle of increase in shear strength with matric suction

For low values of saturation, the angle of increase in shear strength with matric suction($\phi^b$) approximates the angle of internal friction ($\phi'$) (Huang et al., 2020; Wong and Ho, 2000). Additionally, we can represent $\sigma_n$ = weight $\times \cos\alpha$ (Figure 2), where the weight of the sliding block is the unit weight of the soil multiplied by the thickness of the block (weight = $\gamma_t h_s$). Finally, since matric suction ($\psi$) can be written as ($u_a - u_w$), and $u_a = 0$, equation (3) simplifies to:

$$FS = \frac{c' - \psi\tan\phi'}{\gamma_t h_s \sin\alpha} + \frac{\tan\phi'}{\tan\alpha} \tag{4}$$

Substituting equation (4) into equation (1), we can calculate the critical acceleration required to initiate sliding of the soil layer:

$$a_{c,constant} = \frac{c'g - \psi g \tan\phi'}{\gamma_t h_s} + g\cos\alpha\tan\phi' - g\sin\alpha \tag{5}$$

During an earthquake, the soil experiences both vertical ($a_v$) and horizontal ($a_h$) time-variable ground motions. The acceleration normal to the slope ($a_n$), which affects the normal stress and thus, the shear strength, is given by $a_n = a_v(t)\cos\alpha + a_h(t)\sin\alpha$ (Figure 2) (Huang et al., 2020). The transient critical acceleration then becomes:

$$a_{c,transient}(t) = \left(\frac{c'g - g\psi\tan\phi'}{\gamma_t h_s}\right) - g\sin\alpha + \tan\phi'\left(g\cos\alpha - a_v(t)\cos\alpha - a_h(t)\sin\alpha\right) \tag{6}$$

Finally, the downslope sliding acceleration $a_s(t)$, which drives failure, is defined as:

$$a_s(t) = a_h(t)\cos\alpha - a_v(t)\sin\alpha \tag{7}$$

When $a_s(t) > a_{c,transient}(t)$, the driving forces down slope are able to overpower the resistive ones, and the block becomes a candidate for failure.

## 2.2 Model framework and Implementation

*ShallowLandslider* has been implemented in Python utilising the open-source Landlab framework, which provides flexible and modular tools for modelling Earth surface processes on structured grids (Barnhart et al., 2020; Hobley et al., 2017). It offers a general template for creating and manipulating elevation grids, whether imported or generated, and enables easy coupling with hillslope processes, sediment transport and bedrock landsliding. This means that these processes need not be coded within *ShallowLandslider*, being attached as and when necessary. The core calculations are handled on `numpy` arrays, allowing rapid processing and straightforward implementation of spatial variability. Spatial grouping and zonal analysis is performed using tools from `scipy.ndimage`, and model parameters are defined via structured configuration files. The workflow is summarised in Figure 3.

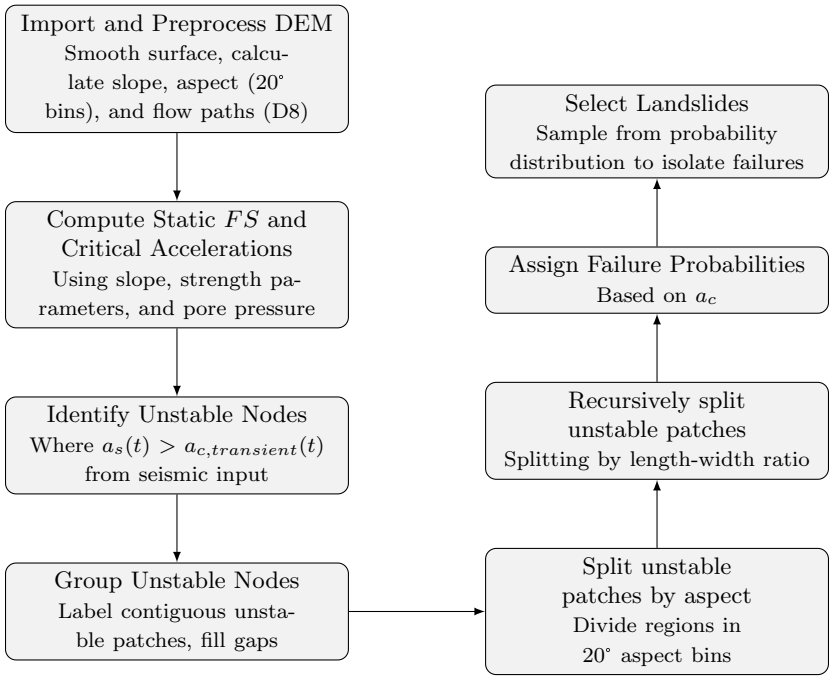


Figure 3: ShallowLandslider workflow showing DEM preprocessing, factor-of-safety calculation, unstable node grouping and shaping, probability assignment, and landslide selection.

### 2.2.1 Model Inputs

**Topographic Data and Preprocessing** Topographic data were derived from the Shuttle Radar Topography Mission (SRTM) digital elevation model (DEM) at 30 m spatial resolution. We chose this resolution because of its wide availability, and its balance between capturing hillslope-scale variability and computational efficiency. In our model runs, the DEM was also imported specifically for running *ShallowLandslider*. However, *ShallowLandslider* is agnostic about the resolution, and is programmed to accept a preprocessed DEM from other Landlab models. Prior to model execution, the DEM was smoothed to remove small artifacts, and primary topographic metrics: slope, aspect, and planform curvature calculated at each grid node. These metrics are subsequently used to define local soil depth patterns and slope stability within *ShallowLandslider*.

**Geotechnical and Seismic Parameters** The model requires a variety of input parameters describing slope geometry, soil mechanical properties, and seismic forcing. Table 1 lists all parameters used in the model, their definitions, units, and any default values.

Spatial distributions of geotechnical parameters, including cohesion ($c'$), effective friction angle ($\phi'$), soil unit weight ($\gamma_t$), and soil thickness ($h_s$) are based on representative values from analyses around the world (Campforts et al., 2022; Huang et al., 2020). Seismic forcing was defined using spatially distributed peak ground accelerations (PGA) derived from the USGS ShakeMap data published for the Gorkha earthquake (USGS, 2015). The resolution of this data was such that there was very little variation between the DEM pixels, allowing us to uniformly apply constant values for the horizontal and vertical acceleration components ($a_h(t)$ and $a_v(t)$) to each node in the model grid. This uniformity also meant that it was significantly simpler computationally. However, due to the gridded nature of the model, variability in PGA can be easily applied for regions where applicable.

### 2.2.2 Model Workflow

At its core, *ShallowLandslider* identifies zones of instability by evaluating Newmark-based critical accelerations at each grid node on the DEM. Grids for the horizontal and vertical components of PGA are used to calculate transient ground accelerations, which are compared to the nodal critical acceleration thresholds to determine areas of instability. These unstable nodes are grouped together into contiguous patches, which are then subdivided based on topographic aspect and aspect ratio. Each patch is assigned a probability of failure based on the median critical acceleration for that patch, enabling stochastic landslide selection. The proportion of patches that fail as landslides is calculated based on a high-percentile threshold of the probability distribution (Figure 3).

**Region splitting** Unstable nodes are first grouped into contiguous regions based on spatial connectivity. To avoid patches having artificial connections across channels and ridgelines, they are split into smaller patches based on topographic aspect. This also allows us to confine the landslides to single slope faces. To do this, the smoothed DEM is segmented into zones of near-constant slope aspect, binned so that each represents a narrow aspect range (i.e., approximating a single slope face). Connected unstable regions are subsequently subdivided according to these aspect zones to yield candidate landslide areas. For each candidate area, the downslope length and cross-slope width are measured and compared to the empirical distribution of length-width ratios from the measured landslide inventory. Areas lying outside this distribution, either where width exceeds length, or where lengths are disproportionately large, are split at their centroid. This process is applied recursively: after each split, the dimensions of all subregions are recalculated, and those still falling outside the empirical range are split again. This continues until at least *75%* of areas conform to the observed length-width relationship.

**Probabilistic landslide selection** Whether a slope is stable or not is a largely deterministic process, which we calculate using the Newmark method. However, whether an unstable area actually develops into a landslide is partly stochastic, partly reflecting natural variability in local conditions not captured by the grid-scale parameters,

such as vegetation, etc. (Meunier et al., 2008; Westen et al., 2008). To represent this natural variability, *ShallowLandslider* implements a probabilistic selection procedure. Each unstable area is assigned a probability of failure ($P_{fail}$) inversely proportional to its critical acceleration, such that higher critical accelerations correspond to lower $P_{fail}$. A weighted random sampler then selects and classifies a subset of unstable areas as landslides. The selection proportion is set to $\bar{P}_{fail} + \sigma P_{fail}$ (i.e., one standard deviation above the mean failure probability) ensuring that the number of selected landslides reflects both central tendency and variability in $P_{fail}$. This approach introduces some stochasticity while biasing the selection toward areas more likely to fail.

In traditional Newmark analyses, the Newmark displacement is usually calculated after identifying unstable areas (Huang et al., 2020; Jibson et al., 2000). This displacement represents the cumulative permanent downslope movement of the sliding block during shaking. *ShallowLandslider* calculates these values for the selected failure nodes and is able to move this sediment downslope along multiple flow paths. However, we have chosen not to use them in this analysis and instead, focused on the identified areas themselves. This choice reflects our emphasis on the spatial patterns of instability rather than on post-failure deformation magnitudes.

### 2.2.3 Numerical configuration and grid setup

Simulations were performed on a structured raster grid matching the resolution of the input DEM (30 m). Each grid node stores elevation, slope, aspect, and soil property values. Boundary nodes were treated as open to prevent artificial instability at domain edges, but were not involved in the calculations. The model supports grids of any spatial resolution, though coarser grids ($> 100\,\mathrm{m}$) may underestimate short-wavelength variability in topographic parameters.

Transient accelerations were computed at each node by applying the time-dependent acceleration functions ($a_h(t)$, $a_v(t)$) to the local slope geometry following equations (6)–(7). The shaking duration of the acceleration record can be specified by the user; in typical simulations, we specify a total shaking duration $T = 10\,\mathrm{s}$ to define the time series of transient accelerations. However, this value is only used to calculate the Newmark displacement for unstable nodes, which are not used in the present analysis. Therefore, the choice of $T$ does not influence our results in any way.

The calculations are vectorized using `NumPy` arrays and executed within the Landlab framework, which handles domain discretization and spatial connectivity. The flow routing is performed using the PriorityFloodFlowRouter component in Landlab. Computations were performed on a standard workstation (e.g., 32 GB RAM, Intel Core i7) with runtimes varying between 15 minutes to an hour for a 648x504 grid, covering a physical area of $\approx 250\,\mathrm{km}^2$. The variability in runtime largely depends on the degree of instability encountered; if there are large swathes of instability to sift through, the model takes longer.

### 2.2.4 Validation setup

We performed a total of 22 simulations, comprising 11 runs for each of the two model subregions. Each simulation was conducted on a grid of similar spatial extent and resolution (30 m), consistent with the input DEM described above. The simulations were designed to explore the sensitivity of modelled slope stability to variations in soil mechanical properties, specifically soil depth ($h_s$) and effective cohesion ($c'$). Different spatial distributions of soil depth were prescribed for each run, together with corresponding adjustments to cohesion values to represent plausible end-member conditions for the study areas. All other parameters, were held constant between runs.

This ensemble of simulations provides a basis for evaluating how well the model reproduces the observed distribution of coseismic landslides given a particular earthquake and regional topographic dataset.

**Landslide inventory data** We validated our model outputs against the coseismic landslide inventory compiled by Roback et al. (2018). They mapped over 24,000 coseismic landslides triggered by the Gorkha earthquake and its aftershocks across central Nepal. The inventory was derived from pre- and post-earthquake high-resolution

optical imagery (WorldView-2, -3 and Pleiades), manually delineated at a general ground sample distance of 20 cm – 50 cm. The dataset is made up of polygonal landslide outlines, classified by failure type and location accuracy.

For our analysis, we clipped the inventory to the two subregions used in our model simulations and rasterized the polygons to the 30 m grid resolution of the input DEM. We excluded polygons that were smaller than a single grid cell, since our model is restricted to the pixel resolution of the DEM. The resulting raster layers were used to calculate the magnitude-frequency statistics, along with the spatial distribution of the observed landslides across elevation, slope, and aspect.

#### 2.2.5 Software environment and reproducibility

*ShallowLandslider* is implemented in `Python 3.12`, building on the open-source Landlab library (Barnhart et al., 2020; Hobley et al., 2017). Core dependencies include `NumPy`, `Pandas`, `SciPy`, `Matplotlib`, and `scikit-image` for numerical computation and visualization. All model parameters, file paths, and runtime options are defined in a structured `JSON` configuration file, which facilitates repeatable simulations and parameter sweeps.

Model code and example input datasets will be made available through an open-access repository (e.g., GitHub or Zenodo) upon publication, ensuring full reproducibility of all results presented in this study.

# 3 Validation

In validating *ShallowLandslider*, we focused on the ability to reproduce the statistical and spatial distribution of landslides rather on determining the exact locations of individual failures. Since slope failures are inherently stochastic, and strongly influenced by local heterogeneities in soil structure, lithology, vegetation, and triggering conditions, a direct pixel-to-pixel comparison between mapped and modelled landslides is of limited diagnostic value, particularly for regional-scale models where variability in these properties exceed landslide dimensions. Instead, we evaluate whether the model is able to reproduce the broad characteristics of the landslide population: the magnitude–frequency behaviour, preferred topographic settings, and spatial concentration within the landscape.

Validation was carried out for two subregions in central Nepal that differ primarily in their topographic signature, and distance from the epicentre of the 2015 earthquake (as described in section 1.1). We restricted the validation to two subregions rather than the entire study area to balance scientific clarity and computational feasibility. Running the model across the full landslide affected region would have substantially increased computational cost, limiting the scope for parameter exploration and sensitivity testing. Focusing on smaller subregions allows for a more detailed assessment of model performance under controlled conditions, and reduces the effect of large-scale variations in topography and seismic forcing.

Despite experiencing similar peak ground accelerations (PGA), the two subregions produced highly contrasting numbers of mapped landslides: 523 in subregion 1 (west) versus 2,353 in subregion 2 (east). The large disparity in landslide density likely reflects differences in relief, slope distribution, and lithology between the two regions. This makes them ideal for evaluating the model's capacity to capture regional variations in landslide susceptibility under near-identical seismic loading. For each subregion, the model was run across a series of parameter combinations representing different soil depths, cohesion values, and angles of internal friction. The landslide populations simulated in each run were then compared with the preprocessed Roback et al. (2018) inventory (Section 1.2.4).

This approach shifts the emphasis of prediction from event-specific to landscape-scale, determining whether *ShallowLandslider* can generate a failure population that is statistically consistent with the observed one in terms of area, elevation, slope, and aspect distributions.

## 3.1 Metrics and Rationale

To quantify the similarity between the modelled and observed landslide distributions, we used two complementary non-parametric statistics: the Kolmogorov–Smirnov (KS) / Kuiper statistic, and the Wasserstein distance. These metrics compare entire probability distributions rather than discrete observations, making them well-suited for evaluating the performance of models designed to reproduce overall distributional characteristics.

The KS statistic represents the maximum vertical distance between the cumulative distribution functions (CDFs) of two datasets. KS values close to zero indicate strong agreement between the observed and modelled landslides amongst the evaluated parameters (i.e., elevation, slope, and area), while higher values indicate increasing divergence. The KS test is widely used in geomorphological and hydrological modelling to evaluate similarity between observed and simulated frequency distributions.

However, since it requires the input data be linear with distinct endpoints, the test cannot be applied to topographic aspect, which is a circular variable (0°–360°, with 0° ≡ 360°). For aspect, we instead use the Kuiper test, a circular analogue of the KS test that is invariant under cyclic transformations and provides a more robust measure for directional data. It is defined as the sum of the maximum positive and negative deviations between two cumulative distribution functions (Fisher, 1993).

The Wasserstein distance, also referred to as the Earth-Mover's Distance, represents the minimum amount of "work" required to transform one distribution into another, corresponding to the area between the two cumulative distribution functions. It is particularly sensitive to systematic offsets between distributions (e.g., if simulated landslides are consistently larger or occur at higher elevations than those observed) (Ramdas et al., 2015; Rubner et al., 2000). Similar to the other metrics, a lower Wasserstein distance indicates stronger agreement between the two distributions. Together, the KS/Kuiper and Wasserstein metrics provide a complementary evaluation: the former emphasizes localised shape differences, while the latter quantifies global biases between distributions.

We computed these metrics for four key variables that collectively describe the statistical structure of the landslide population: landslide area, mean elevation, mean slope, and mean aspect. Each of these statistical comparisons were performed on normalised cumulative distributions to eliminate scale effects between variables.

## 3.2 Soil depth configuration and parametrisation

Soil depth ($h_s$) exerts a first-order control on slope stability by influencing both the driving gravitational stress and the potential for pore-pressure generation during seismic shaking.

Within *ShallowLandslider*, $h_s$ directly affects the factor of safety via its modulation of the ratio of resisting to driving forces (Eq. 2). Consequently, even modest variations in $h_s$ can substantially alter the predicted failure distribution. To evaluate this sensitivity, we tested five soil depth configurations:

1. Uniform: A single, constant soil depth of $h_s = 1\,\text{m}$ is applied across all DEM nodes. This represents a simple baseline scenario, to serve as a reference for comparing more realistic distributions. While easy to implement, it ignores natural variations in soil accumulation and erosion.

2. Elevation-dependent: Soil depth decreases linearly with elevation, from a maximum $h_{s,\max} = 1.5\,\text{m}$ at the lowest elevations, to $h_{s,\min} = 0\,\text{m}$ at the highest. Nodes at the lowest elevations receive the most soil, while those at the top received $h_{s,min} = 0\,\text{m}$. This reflects observed patterns of soil thinning on steep, high-elevation ridges due to enhanced erosion and reduced deposition, with lower-elevation areas accumulating thicker soils (citation).

3. Drainage area-dependent: Soil depth is proportional to the upstream contributing area of each DEM node, calculated from flow routing. Nodes in convergent terrain (hollows and valley floors) receive thicker soils, while divergent or ridge-top areas remain thin. This captures the tendency for colluvial deposits to accumulate in topographic lows (Catani et al., 2010; Park et al., 2001), making these zones more prone

to failure. By accounting for hydrologic connectivity, this approach links soil thickness to landscape-scale sediment transport processes.

4. Curvature-dependent: Soil depth ($h_s$) was modulated according to the planform curvature ($\kappa$) at each DEM node, reflecting the tendency for soil to accumulate in concave topography, and thin on convex slopes. Empirically, concave areas (negative curvature) concentrate soil due to convergent surface processes, while convex ridges (positive curvature) experience enhanced erosion, resulting in thinner soils. Dietrich et al. (1995) and Heimsath et al. (1997) proposed a logarithmic relationship between soil depth and curvature of the form:

$$h_s(\kappa) = -h_* \ln \frac{D\kappa}{P_0} \tag{8}$$

where $h_0$ is a scaling parameter, $D$ is a constant transport coefficient, and $P_0$ is the maximum rate of soil production (i.e., at bare bedrock). This formulation captures the rapid increase in soil depth in concave hollows, and the reduction on convex slopes, and has been widely adopted in process-based soil production and landslide models. However, it diverges for negative curvature values and requires piecewise adjustments: the logarithmic relationship is typically used for $\kappa > 0$, (and in this formulation, when $0 < \frac{D\kappa}{P_0} < 1$), $h_s = h_{min}$ when $\kappa \leq 0$ (Dietrich et al., 1995; Heimsath et al., 1997). While accurate locally, this approach complicates implementation across large landscapes.

Following Patton et al. (2018), we implemented a linear approximation:

$$h_s(\kappa) = \bar{h} + \beta\kappa \tag{9}$$

where $h_s(\kappa)$ is soil depth, $\kappa$ is planform curvature, $\bar{h}$ is the mean regional soil depth, and $\beta = -446.3\sigma_\kappa + 30.3$ scales the linear relationship based on the standard deviation of curvature (Patton et al., 2018). As with the logarithmic approach, concave areas receive thicker soils, and convex thinner, but this method avoids the divergence issues and allows easy application over the entire DEM.

5. Elevation-weighted Curvature-dependent: The soil depth at each node is calculated as the mean of the soil thicknesses derived from the elevation ($h_{s,\text{elev}}$) and curvature-dependent ($h_{s,\kappa}$) methods. The elevation-dependent term introduces a broad-scale trend of soil thinning with increasing elevation, with the curvature-dependence adds the finer-scale variability.

For each configuration, we ran the model across both subregions to examine whether the influence of $h_s$ was consistent under varying seismic intensities and terrain characteristics. Model performance was evaluated using the KS, Kuiper, and Wasserstein metrics for landslide area, mean slope, mean elevation, and aspect.

## 3.3 Model performance and sensitivity

To evaluate model performance and parameter sensitivity, we ran *ShallowLandslider* for both subregions using the full suite of soil-depth configurations and a range of effective cohesion values ($c' = 0$–$20\,\text{kPa}$). In the following analysis, we focus on three representative sets of simulations from the 22 runs described in Section 1.2.4: (i) the Uniform soil depth configuration, (ii) the Inverse-elevation soil depth configuration with varying cohesion values, and (iii) the Elevation-weighted Curvature-dependent soil depth configuration. These three sets capture the primary patterns of soil depth variability and mechanical strength explored in our ensemble, and provide a clear basis for comparing modelled landslide distributions with observed inventories across both subregions.

Across both subregions, the overall behaviour of the model was consistent: the spatial pattern and total number of simulated landslides were strongly controlled by the assumed soil depth distribution, while variations in effective cohesion ($c'$) modulated the likelihood of failure across steeper slopes and higher elevations. Figures 4 and 5 illustrate the empirical cumulative distribution functions (ECDFs) and histograms of landslide area,

elevation, and slope for the three primary soil depth configurations: Uniform, Inverse-elevation, and Elevation-weighted curvature, together with their mapped counterparts.

The *Uniform* soil depth configuration, although unrealistic, provides a useful baseline for assessing relative model behaviour. At $c' = 15\,\text{kPa}$, the Uniform configuration produced failures that were broadly distributed across the landscape but lacked the topographic clustering observed in the mapped inventory. The absence of any spatial variation highlights the importance of including realistic variations in soil depth (Fig. 4, panel A; Fig. 5, panel A).

Varying cohesion within the inverse-elevation soil depth configuration revealed important systematic trends. In both subregions, increasing $c'$ reduced the number of predicted landslides and shifted their distribution toward steeper slopes and higher elevations, with the highest values ($c' > 20\,\text{kPa}$) suppressing failures almost entirely. Cohesion values in the range 10–15 kPa provided the closest match to the mapped inventories, with minimal KS/Kuiper metrics and Wasserstein distances across slope, elevation and aspect (Figs. 6–7).

In subregion 1, the Inverse-elevation configuration performed best overall, particularly for the slope, elevation and topographic aspect distributions (Figures 4, panel B; 6). At $c' = 10\,\text{kPa}$, the model yielded KS values of 0.095 and 0.084, and Wasserstein distances of 0.071 and 0.104 for elevation and slope, respectively. In terms of aspect, it was also one of the best performing models, with a Kuiper metric of 0.156. However, it tended to overestimate landslide areas ($KS = 0.442$, $W = 0.411$). The elevation-weighted curvature configuration, in contrast, improved the area distribution significantly ($KS = 0.190$, $W = 0.07$) and performed comparably for slope, though it overpredicted the mean elevation of failures ($KS = 0.484$, $W = 0.613$) (Figures 4, panel C; 6). Overall, the western subregion exhibited high sensitivity to the assumed soil depth pattern, with the Inverse-elevation configuration capturing most of the observed topographic signal at moderate cohesion.

In subregion 2, model performance shifted toward stronger influence of local topography. Here, the Elevation-weighted Curvature configuration consistently outperformed all others (Fig. 5, panel C), producing some of the lowest KS/Kuiper and Wasserstein statistics for area ($KS = 0.30$; $W = 0.123$), elevation ($KS = 0.165$; $W = 0.186$), slope ($KS = 0.065$; $W = 0.071$), and aspect (Kuiper = 0.192) at $c' = 15\,\text{kPa}$ (Fig. 7). Although not the absolute lowest values, this configuration provided the best overall fit. In contrast, the Inverse-elevation model, which was most successful in subregion 1, performed notably worse here, even with variable values of $c'$, failing even to reproduce the mean elevations well (Fig. 7).

Additional configurations tested including the drainage-area-dependent and simple curvature-dependent models, exhibited intermediate behaviour. In subregion 1, they were equally as bad at reproducing the elevation distributions as the Elevation-weighted curvature model, but performed significantly worse at reproducing the aspect distributions ((Kuiper $= 0.214 - 0.229$)) (Fig. 6). They are better in subregion 2, where they are able to reproduce the mean elevations and slopes very well ($KS = 0.099 - 0.188$; $W = 0.1 - 0.206$). They still failed to reproduce the aspect distribution, however, with the Kuiper metric varying between $0.192 - 0.251$ (Fig. 7). The simple curvature-based models were very good at reproducing the area distributions, as shown in both subregions, a feature inherited by the combined Elevation-weighted Curvature model.

Taken together, these experiments demonstrate that *ShallowLandslider* is capable of reproducing the observed statistical and topographic characteristics of regional landslide populations when both soil depth and material strength are realistically parameterized. While optimal parameter combinations differ slightly between subregions, reflecting local differences in terrain morphology and sediment storage, the consistent improvement achieved with curvature-modulated soil depths and moderate cohesion values (10–15 kPa) indicates that these factors capture the dominant physical controls on shallow failure initiation under seismic loading in central Nepal.

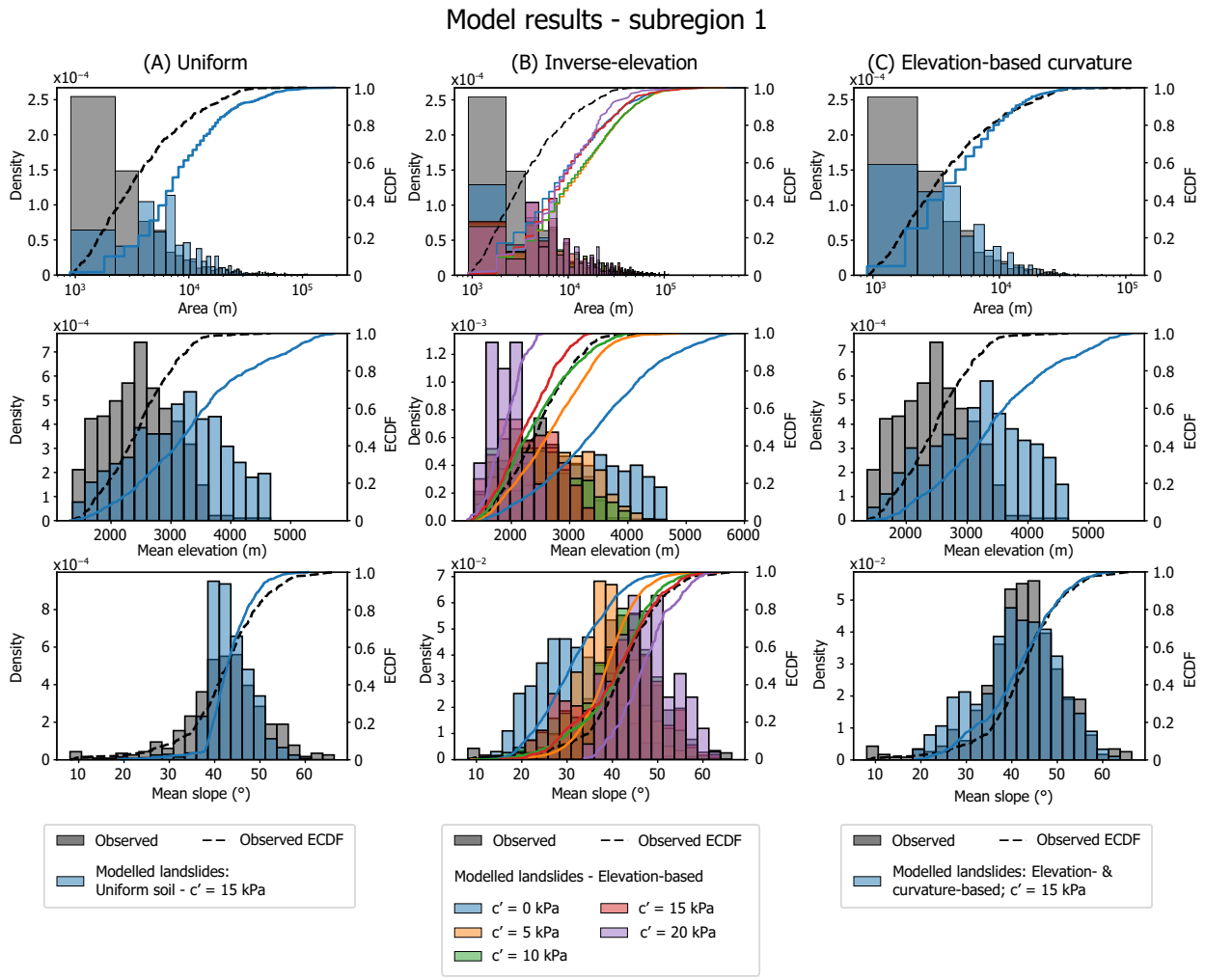


Figure 4: Histograms and empirical cumulative distribution functions (ECDFs) for each model run in Subregion 1 (west). (A) Histograms and ecdf for models with 1 m soil depth uniformly distributed over the entire region. (B) Histograms and ecdfs for models with soil depth inversely proportional to elevation. Grey histogram and black dashed line show observed distribution. Colours are for different effective cohesion values. (C) Histograms and ecdfs for models using the elevation-based curvature to calculate the soil depth.

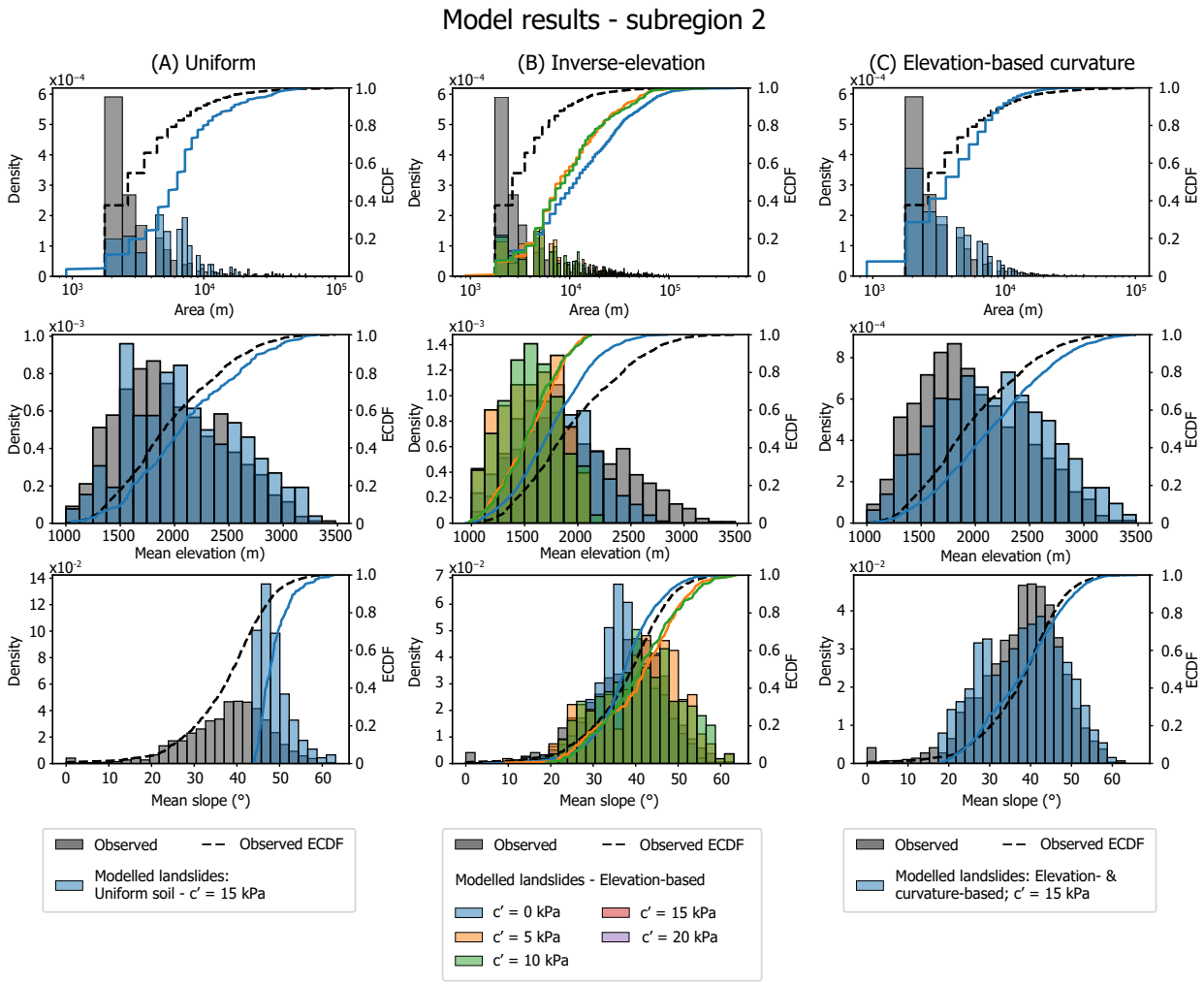


Figure 5: Histograms and empirical cumulative distribution functions (ECDFs) for each model run in Subregion 1 (west). (A) Histograms and ecdf for models with 1 m soil depth uniformly distributed over the entire region. (B) Histograms and ecdfs for models with soil depth inversely proportional to elevation. Grey histogram and black dashed line show observed distribution. Colours are for different effective cohesion values. (C) Histograms and ecdfs for models using the elevation-based curvature to calculate the soil depth.

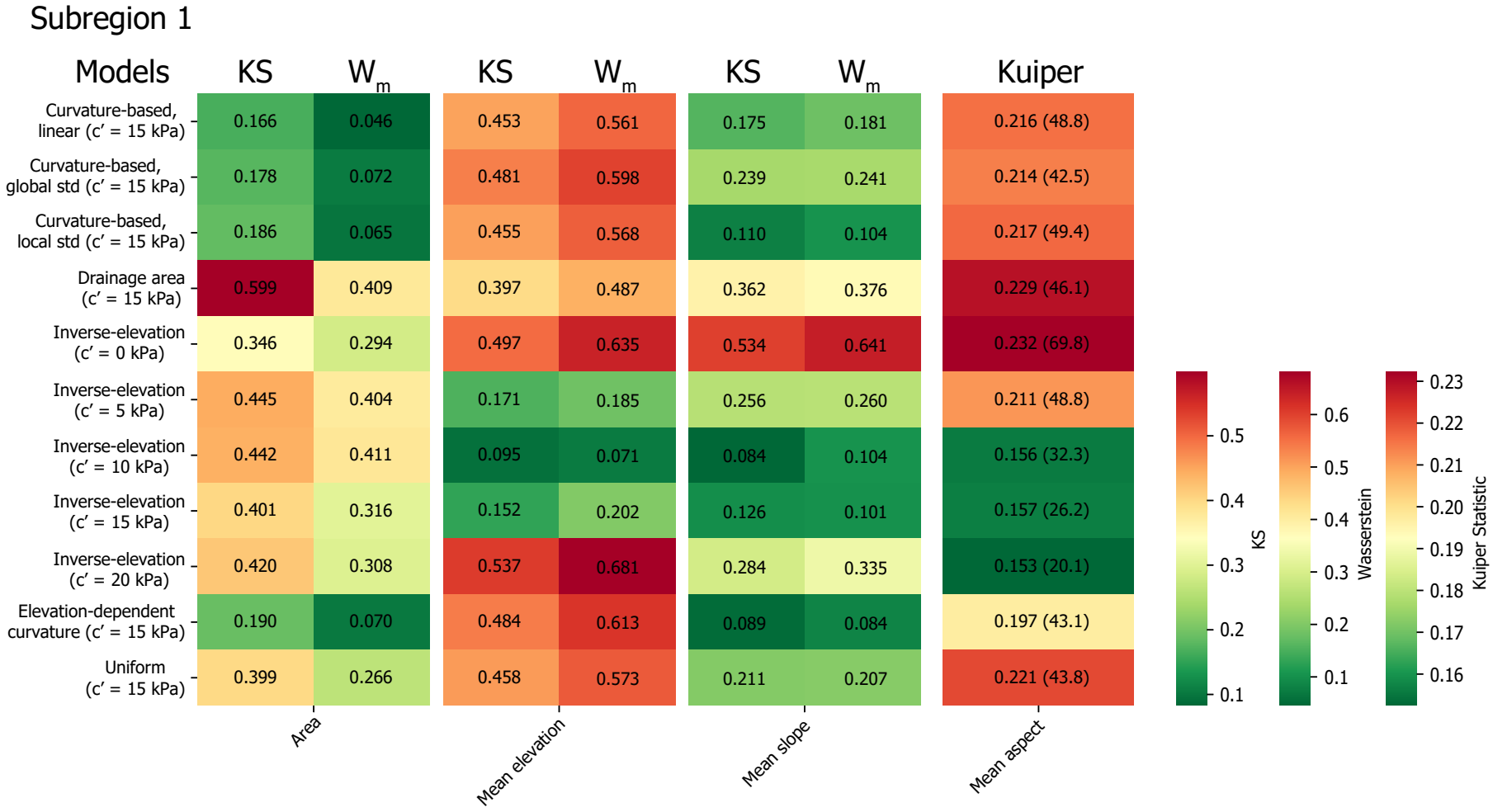


Figure 6: Model performance heatmaps for subregion 1 (west), comparing modelled versus observed elevation, slope and landslide areas. (A) Heatmap showing Kolmogorov-Smirnov statistic for each model run; (B) Heatmap showing Wasserstein distance for each model run; (C) Heatmap showing Size ratio for each model run; (D) Heatmap showing Kuiper statistic for topographic aspect, with the difference between the mean modelled and observed aspect in brackets.

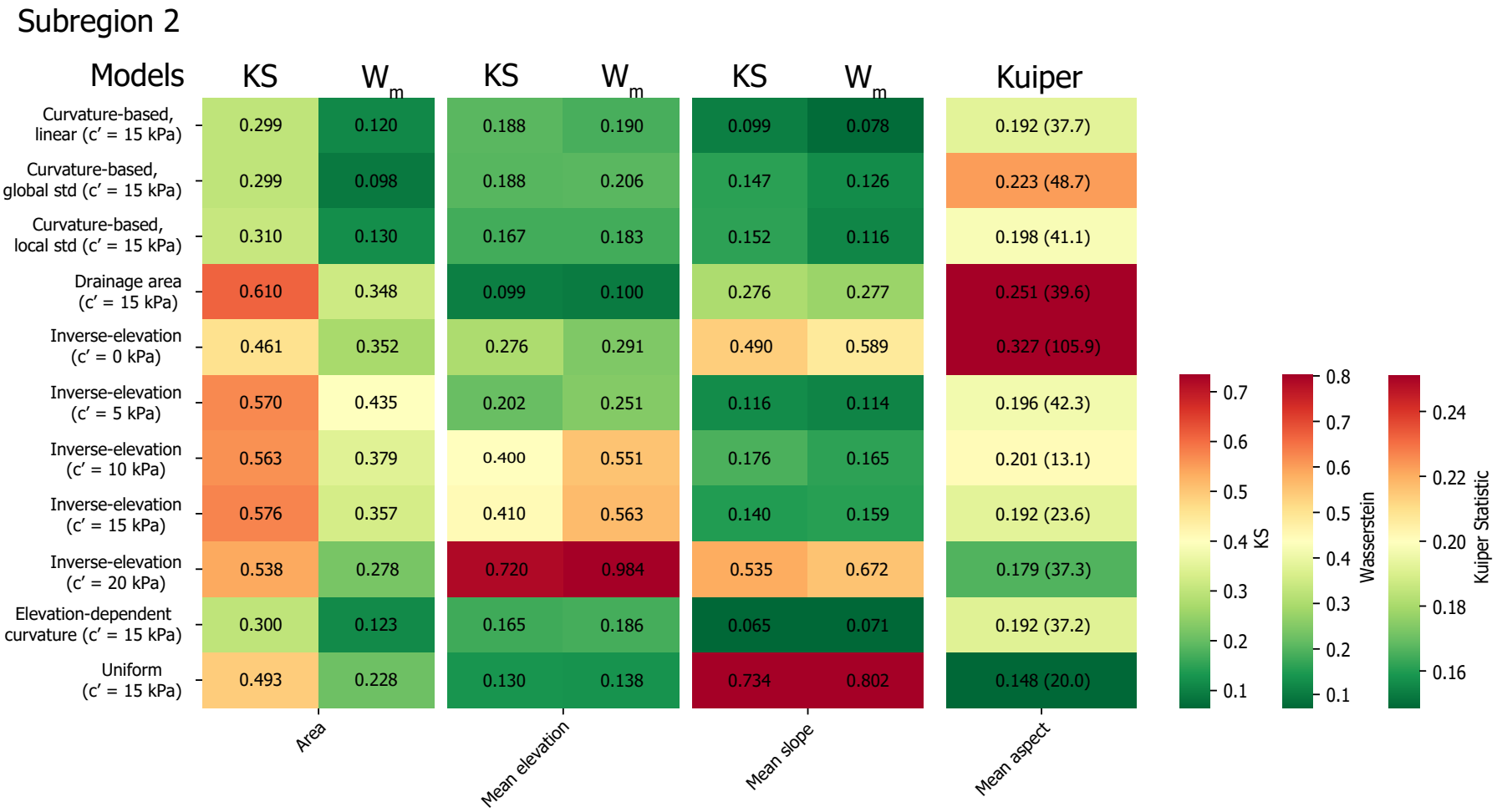


Figure 7: Model performance heatmaps for subregion 2 (south), comparing modelled versus observed elevation, slope and landslide areas. (A) Heatmap showing Kolmogorov-Smirnov statistic for each model run; (B) Heatmap showing Wasserstein distance for each model run; (C) Heatmap showing Size ratio for each model run; (D) Heatmap showing Kuiper statistic for topographic aspect, with the difference between the mean modelled and observed aspect in brackets.

# 4 Discussion

## 4.1 Model performance and validation

*ShallowLandslider* was designed to reproduce the statistical and spatial characteristics of earthquake-triggered shallow landslide populations at regional scales. Validation against mapped inventories in two subregions of central Nepal demonstrates that the model successfully captures key aspects of landslide populations, including size distributions, slope and elevation preferences, and topographic aspect. In subregion 1, the Inverse-elevation soil-depth configuration provided the closest match for slope and elevation distributions, while the Elevation-weighted Curvature configuration improved reproduction of landslide areas. In subregion 2, the Elevation-weighted Curvature configuration generally outperformed all other tested soil-depth distributions, highlighting the importance of representing fine-scale topographic variability in complex terrain (Figures 1–2).

Performance metrics reinforce these qualitative observations. Across both subregions, KS, Kuiper, and Wasserstein metrics showed that moderate cohesion values ($c' = 10$ – $15\,\mathrm{kPa}$) and realistic soil-depth variability yielded the closest correspondence with observed landslide distributions. While some metrics (e.g., landslide area) remained challenging to reproduce perfectly, the model captures first-order patterns in topography and failure propensity. By focusing on population-level statistics rather than exact pixel-level prediction, *ShallowLandslider* provides a robust and practical tool for regional hazard assessment.

## 4.2 Controls on model behaviour

Model behaviour in *ShallowLandslider* reflects the combined influence of material parameters, topographic variability, and seismic forcing. Among these, soil depth ($h_s$) exerts the strongest control on both the number and spatial distribution of simulated landslides. Variations in $h_s$ directly alter the driving-to-resisting force ratio across the landscape, effectively setting the pattern of potential instability. Uniform soil depths, although useful as a baseline, fail to reproduce the observed topographic clustering of failures, effectively reducing the topographic variability of the region. This underscores the importance of introducing realistic spatial variability in soil thickness for any regional-scale slope stability model.

The Inverse-elevation configuration captured broad-scale patterns in subregion 1, successfully reproducing slope and elevation distributions. However, this approach proved insufficient in subregion 2, where curvature-modulated soil-depth configurations were essential to reproduce observed landslide clustering and aspect patterns, highlighting the need to represent microtopographic variability in complex landscapes.

Effective cohesion ($c'$) also plays a critical role by modulating the likelihood of failure, particularly along steep slopes and ridgelines. Across all tested configurations, intermediate cohesion values ($c' = 10$–$15\,\mathrm{kPa}$) provided the closest match to mapped inventories, while both lower and higher values produced unrealistic landslide densities. This range is consistent with general estimates for colluvial soils in similar settings (Campforts et al., 2022).

Topography further interacts with seismic forcing to produce distinct regional responses. Despite similar peak ground accelerations (PGA) across the two subregions, observed and simulated landslide densities differ substantially, implying that terrain morphology controls failure susceptibility. Highly dissected, convergent hillslopes amplify local instability by concentrating both stress and soil accumulation, whereas smoother terrain with more uniform slopes exhibits fewer failures under equivalent seismicity.

Finally, the input DEM resolution (30 m SRTM) constrains the minimum size of predicted failures and influences curvature estimates. While finer-resolution topography would improve representation of small-scale terrain variability, relative performance across soil-depth configurations remains consistent, suggesting that the dominant controls captured here are robust to modest changes in grid scale. Overall, these results highlight that accurate simulation of regional landslide populations depends more on representing realistic spatial heterogeneity in soil and topography than on precise tuning of material strength or shaking intensity.

### 4.3 Dependence of soil depth on topographic curvature

Soil thickness is widely recognised as a first-order control on shallow landsliding (Dietrich et al., 2008), yet representing it accurately in basin-scale slope stability models remains challenging. Many regional models rely on simplistic approaches, such as assuming uniform soil depth, using soil classes, or deriving depth from a single topographic attribute such as slope or elevation (Revellino et al., 2008; Saulnier et al., 1997; Segoni et al., 2012). These approaches are easy to implement but may fail to capture landscape-scale heterogeneity that strongly influences landslide initiation.

Process-based approaches, such as those of Dietrich et al. (1995) and Roering (2008), simulate soil thickness by evolving landscapes forward in time using numerical landscape evolution models, starting from modern topography and an assumed initial soil thickness. These models integrate soil production, hillslope erosion, and non-linear depth- and slope-dependent transport to generate spatially distributed soil thickness predictions. While physically grounded, these methods require high-resolution topographic data, assumptions about uplift rates, initial conditions, and long-term landscape evolution, which limit their general applicability for regional-scale hazard modelling (Pelletier and Rasmussen, 2009).

To explore the influence of different parametrisations, we tested several soil-depth configurations, including uniform, elevation-dependent, curvature-dependent, and the hybrid Elevation-weighted Curvature model. The uniform configuration produced homogenous spatial patterns and failed to reproduce the observed clustering of landslides, particularly along convergent hillslopes and valley heads. Elevation-based models performed moderately well, accurately reproducing expected elevation and slope distributions, but failing to simulate the observed magnitude-frequency distributions.

Planform curvature has been widely used as a first-order predictor of soil thickness because concave areas tend to accumulate thicker soils, whereas convex ridges are eroded and remain thin (Dietrich et al., 1995; Heimsath et al., 1997; Patton et al., 2018). In our simulations, we used the linear relationship between curvature and soil depth proposed by Patton et al. (2018). We find that curvature-based approaches were best at reproducing the observed magnitude-frequency distribution. However, in subregion 1 using curvature alone does not fully capture the observed landslide patterns. Simple curvature-based soil-depth configurations underestimated accumulation in low-elevation convergent areas and overestimated it on high ridges. It also leads to more failures occurring on differently facing slopes, leading to a large mismatch in the topographic aspect.

The Elevation-weighted Curvature configuration improves upon this slightly by combining local curvature with a broad elevation-dependent trend, producing more realistic soil-depth distributions across heterogeneous terrain. Concave, low-elevation areas accumulate thicker soils, producing landslide clustering that aligns well with observations, while convex ridges remain thin and stable. This configuration generally outperformed uniform, elevation-only, and simple curvature-based models, highlighting that while curvature is an important first-order control, it must be contextualised within larger landscape gradients to accurately capture regional-scale patterns of shallow landsliding. However, the benefits of using this combined approach are limited, as it is also unable to properly simulate the correct elevation distribution for subregion 1.

These results suggest that while curvature is definitely a first-order predictor of soil thickness, hybrid approaches such as Elevation-weighted Curvature provide a practical compromise between process-based rigour and computational tractability in cases of complex terrain.

## 5 Conclusions and Future developments

*ShallowLandslider* extends the framework of Newmark-based and infinite-slope models (e.g., Huang et al., 2020; Jibson, 2007; Montgomery and Dietrich, 1994; Newmark, 1965) toward regional, population-level applications. By combining Newmark-based critical accelerations with stochastic regional failure selection and flexible soil-depth parameterization, it bridges deterministic mechanics and probabilistic realism. The model reproduces

observed landscape-scale landslide statistics without requiring pixel-level precision, which is often unattainable in heterogeneous, seismically disturbed terrain.

Within the broader Landlab modelling ecosystem, *ShallowLandslider* complements existing components that address related slope processes. *LandslideProbability* implements a probabilistic and hydrologic approach for rainfall- or groundwater-induced failures, while *BedrockLandslider* focuses on deep-seated, bedrock-dominated mass movements. Together, these tools span a continuum of slope-failure mechanisms within a unified, grid-based framework. This interoperability enables researchers to explore how distinct triggering processes and material domains interact across spatial and temporal scales.

Future developments of *ShallowLandslider* will focus on expanding its flexibility and integration within broader Earth surface modelling frameworks. Because the model is implemented as a modular Landlab component, it can be readily coupled with existing process models for hydrology, sediment transport, and landscape evolution. This modular design enables straightforward extension to other triggering mechanisms, such as rainfall-driven pore pressure or transient saturation, allowing the simulation of both rainfall- and earthquake-induced shallow landslides within a consistent physical framework. Another promising direction is the coupling of *ShallowLandslider* with dynamic rupture models that simulate realistic, spatially variable ground motion fields. State-of-the-art tools such as SeisSol (Ulrich et al., 2019) and the recently developed PyQuake3D (Tang et al., 2025) compute 3D dynamic rupture and wave propagation, capturing the effects of fault geometry, topography, and near-surface amplification on shaking intensity. Integrating these outputs with *ShallowLandslider* would enable regionally distributed, physics-based simulations of earthquake-triggered landslides driven by realistic ground motions. Together, these developments point toward a fully coupled, open-source modelling framework that links tectonic processes, surface hydrology, and slope stability within the Landlab ecosystem.

From an applied standpoint, the model offers a practical tool for probabilistic hazard assessment in data-scarce mountainous regions. Sensitivity analyses indicate that moderate variations in uncertain parameters (soil depth, cohesion) do not obscure first-order spatial and statistical trends, supporting the model's robustness and transferability. Nonetheless, limitations remain. Soil-depth distributions are approximations constrained by limited field data; DEM resolution restricts representation of fine-scale topography; and cohesion sensitivity was explored only for one configuration. The Newmark formulation also assumes rigid-block behaviour and neglects progressive failure processes. Future developments incorporating finer-resolution data, improved soil-depth parameterizations, and dynamic hydrologic or seismic feedbacks will enhance predictive realism and broaden applicability.

Overall, *ShallowLandslider* provides a physically grounded, computationally efficient foundation for regional-scale landslide hazard modelling. Its modular design and demonstrated sensitivity behaviour establish a basis for future extensions toward coupled, probabilistic simulations of landscape response to multiple triggers in tectonically and climatically active regions.

# References


Avouac, J.-P. P. et al. (2015). "Lower Edge of Locked Main Himalayan Thrust Unzipped by the 2015 Gorkha Earthquake". In: *Nature Geoscience* 8.9, pp. 708–711. ISSN: 17520908. DOI: 10.1038/ngeo2518.

Barnhart, K. R. et al. (2020). "Short Communication: Landlab v2.0: A Software Package for Earth Surface Dynamics". In: *Earth Surface Dynamics* 8.2, pp. 379–397. ISSN: 2196632X. DOI: 10.5194/esurf-8-379-2020.

Campforts, B. et al. (Aug. 2020). "HyLands 1.0: A Hybrid Landscape Evolution Model to Simulate the Impact of Landslides and Landslide-Derived Sediment on Landscape Evolution". In: *Geoscientific Model Development* 13.9, pp. 3863–3886. ISSN: 1991-9603. DOI: 10.5194/gmd-13-3863-2020. (Visited on 01/02/2024).

Campforts, B. et al. (Aug. 2022). "The Art of Landslides: How Stochastic Mass Wasting Shapes Topography and Influences Landscape Dynamics". In: *Journal of Geophysical Research: Earth Surface* 127.8, e2022JF006745. ISSN: 2169-9003, 2169-9011. DOI: 10.1029/2022JF006745. (Visited on 01/02/2024).

Catani, F., S. Segoni, and G. Falorni (2010). "An Empirical Geomorphology-Based Approach to the Spatial Prediction of Soil Thickness at Catchment Scale". In: *Water Resources Research* 46.5. ISSN: 1944-7973. DOI: 10.1029/2008WR007450. (Visited on 11/12/2025).

Cho, S. and S. Lee (2002). "Evaluation of Surficial Stability for Homogeneous Slopes Considering Rainfall Characteristics". In: *Journal of Geotechnical and Geoenvironmental Engineering* 128.9, pp. 756–763. DOI: 10.1061/(ASCE)1090-0241(2002)128:9(756).

Dahal, A. et al. (Nov. 2024). "Quantifying the Influence of Topographic Amplification on the Landslides Triggered by the 2015 Gorkha Earthquake". In: *Communications Earth & Environment* 5.1, p. 678. ISSN: 2662-4435. DOI: 10.1038/s43247-024-01822-9. (Visited on 11/13/2025).

Dietrich, W. E. et al. (2008). "The Prediction of Shallow Landslide Location and Size Using a Multidimensional Landslide Analysis in a Digital Terrain Model". In: *Proceedings of the Fourth International Conference on Debris-Flow Hazards Mitigation*.

Dietrich, W. E. et al. (Apr. 1995). "A Process-based Model for Colluvial Soil Depth and Shallow Landsliding Using Digital Elevation Data". In: *Hydrological Processes* 9.3-4, pp. 383–400. ISSN: 0885-6087, 1099-1085. DOI: 10.1002/hyp.3360090311. (Visited on 09/04/2025).

Fan, X. et al. (June 2019). "Earthquake-Induced Chains of Geologic Hazards: Patterns, Mechanisms, and Impacts". In: *Reviews of Geophysics* 57.2, pp. 421–503. ISSN: 8755-1209, 1944-9208. DOI: 10.1029/2018RG000626. (Visited on 04/25/2024).

Fisher, N. I. (Oct. 1993). *Statistical Analysis of Circular Data*. 1st ed. Cambridge University Press. ISBN: 978-0-521-35018-1 978-0-521-56890-6 978-0-511-56434-5. DOI: 10.1017/CBO9780511564345. (Visited on 10/13/2025).

Gariano, S. L. and F. Guzzetti (Nov. 2016). "Landslides in a Changing Climate". In: *Earth-Science Reviews* 162, pp. 227–252. ISSN: 0012-8252. DOI: 10.1016/j.earscirev.2016.08.011. (Visited on 11/11/2025).

Heimsath, A. M. et al. (July 1997). "The Soil Production Function and Landscape Equilibrium". In: *Nature* 388.6640, pp. 358–361. ISSN: 0028-0836, 1476-4687. DOI: 10.1038/41056. (Visited on 10/02/2024).

Hobley, D. E. et al. (2017). "Creative Computing with Landlab: An Open-Source Toolkit for Building, Coupling, and Exploring Two-Dimensional Numerical Models of Earth-surface Dynamics". In: *Earth Surface Dynamics* 5.1, pp. 21–46. ISSN: 2196632X. DOI: 10.5194/esurf-5-21-2017.

Hovius, N. et al. (Apr. 2011). "Prolonged Seismically Induced Erosion and the Mass Balance of a Large Earthquake". In: *Earth and Planetary Science Letters* 304.3-4, pp. 347–355. ISSN: 0012821X. DOI: 10.1016/j.epsl.2011.02.005. (Visited on 11/11/2025).

Huang, D. et al. (May 2020). "An Integrated SEM-Newmark Model for Physics-Based Regional Coseismic Landslide Assessment". In: *Soil Dynamics and Earthquake Engineering* 132, p. 106066. ISSN: 02677261. DOI: 10.1016/j.soildyn.2020.106066. (Visited on 05/09/2024).

Ingles, J., J. Darrozes, and J.-C. Soula (Aug. 2006). "Effects of the Vertical Component of Ground Shaking on Earthquake-Induced Landslide Displacements Using Generalized Newmark Analysis". In: *Engineering Geology* 86.2-3, pp. 134–147. ISSN: 00137952. DOI: 10.1016/j.enggeo.2006.02.018. (Visited on 04/01/2025).

Jibson, R. W., E. L. Harp, and J. A. Michael (Dec. 2000). "A Method for Producing Digital Probabilistic Seismic Landslide Hazard Maps". In: *Engineering Geology* 58.3-4, pp. 271–289. ISSN: 00137952. DOI: 10.1016/S0013-7952(00)00039-9. (Visited on 02/19/2025).

Jibson, R. W. (May 2007). "Regression Models for Estimating Coseismic Landslide Displacement". In: *Engineering Geology* 91.2-4, pp. 209–218. ISSN: 00137952. DOI: 10.1016/j.enggeo.2007.01.013. (Visited on 02/26/2025).

Kargel, J. S. et al. (Dec. 2015). "Geomorphic and Geologic Controls of Geohazards Induced by Nepal's 2015 Gorkha Earthquake". In: *Science* 351.6269, aac8353. ISSN: 0036-8075, 1095-9203. DOI: 10.1126/science.aac8353. (Visited on 04/23/2025).

Keefer, D. K. (Apr. 1984). "Landslides Caused by Earthquakes". In: *GSA Bulletin* 95.4, pp. 406–421. ISSN: 0016-7606. DOI: 10.1130/0016-7606(1984)95<406:LCBE>2.0.CO;2. (Visited on 11/11/2025).

Kritikos, T., T. R. Robinson, and T. R. H. Davies (2015). "Regional Coseismic Landslide Hazard Assessment without Historical Landslide Inventories: A New Approach". In: *Journal of Geophysical Research: Earth Surface* 120.4, pp. 711–729. ISSN: 2169-9011. DOI: 10.1002/2014JF003224. (Visited on 08/13/2025).

Lombardo, L. et al. (Oct. 2020). "Space-Time Landslide Predictive Modelling". In: *Earth-Science Reviews* 209, p. 103318. ISSN: 00128252. DOI: 10.1016/j.earscirev.2020.103318. (Visited on 12/31/2023).

Meena, S. R. and S. Tavakkoli Piralilou (Oct. 2019). "Comparison of Earthquake-Triggered Landslide Inventories: A Case Study of the 2015 Gorkha Earthquake, Nepal". In: *Geosciences* 9.10, p. 437. ISSN: 2076-3263. DOI: 10.3390/geosciences9100437. (Visited on 06/04/2025).

Meunier, P., N. Hovius, and J. A. Haines (Nov. 2008). "Topographic Site Effects and the Location of Earthquake Induced Landslides". In: *Earth and Planetary Science Letters* 275.3-4, pp. 221–232. ISSN: 0012821X. DOI: 10.1016/j.epsl.2008.07.020. (Visited on 09/30/2024).

Montgomery, D. R. and W. E. Dietrich (Apr. 1994). "A Physically Based Model for the Topographic Control on Shallow Landsliding". In: *Water Resources Research* 30.4, pp. 1153–1171. ISSN: 0043-1397, 1944-7973. DOI: 10.1029/93WR02979. (Visited on 03/12/2024).

Newmark, N. M. (June 1965). "Effects of Earthquakes on Dams and Embankments". In: *Géotechnique* 15.2, pp. 139–160. ISSN: 0016-8505, 1751-7656. DOI: 10.1680/geot.1965.15.2.139. (Visited on 03/19/2025).

Nowicki Jessee, M. A. et al. (2018). "A Global Empirical Model for Near-Real-Time Assessment of Seismically Induced Landslides". In: *Journal of Geophysical Research: Earth Surface* 123.8, pp. 1835–1859. ISSN: 2169-9011. DOI: 10.1029/2017JF004494. (Visited on 11/06/2025).

Park, S. J., K. McSweeney, and B. Lowery (Oct. 2001). "Identification of the Spatial Distribution of Soils Using a Process-Based Terrain Characterization". In: *Geoderma* 103.3, pp. 249–272. ISSN: 0016-7061. DOI: 10.1016/S0016-7061(01)00042-8. (Visited on 11/12/2025).

Parker, R. N. et al. (Oct. 2015). "Spatial Distributions of Earthquake-Induced Landslides and Hillslope Preconditioning in the Northwest South Island, New Zealand". In: *Earth Surface Dynamics* 3.4, pp. 501–525. ISSN: 2196-632X. DOI: 10.5194/esurf-3-501-2015. (Visited on 08/13/2025).

Patton, N. R. et al. (Aug. 2018). "Predicting Soil Thickness on Soil Mantled Hillslopes". In: *Nature Communications* 9.1, p. 3329. ISSN: 2041-1723. DOI: 10.1038/s41467-018-05743-y. (Visited on 07/10/2024).

Pelletier, J. D. and C. Rasmussen (2009). "Geomorphically Based Predictive Mapping of Soil Thickness in Upland Watersheds". In: *Water Resources Research* 45.9. ISSN: 1944-7973. DOI: 10.1029/2008WR007319. (Visited on 08/13/2025).

Petley, D. (Oct. 2012). "Global Patterns of Loss of Life from Landslides". In: *Geology* 40.10, pp. 927–930. ISSN: 1943-2682, 0091-7613. DOI: 10.1130/G33217.1. (Visited on 11/11/2025).

Ramdas, A., N. Garcia, and M. Cuturi (2015). "On Wasserstein Two-Sample Testing and Related Families of Nonparametric Tests". In: arXiv: 1509.02237 [math.ST].

Reichenbach, P. et al. (May 2018). "A Review of Statistically-Based Landslide Susceptibility Models". In: *Earth-Science Reviews* 180, pp. 60–91. ISSN: 0012-8252. DOI: 10.1016/j.earscirev.2018.03.001. (Visited on 08/13/2025).

Revellino, P., F. M. Guadagno, and O. Hungr (Feb. 2008). "Morphological Methods and Dynamic Modelling in Landslide Hazard Assessment of the Campania Apennine Carbonate Slope". In: *Landslides* 5.1, pp. 59–70. ISSN: 1612-5118. DOI: 10.1007/s10346-007-0103-2. (Visited on 11/05/2025).

Roback, K. et al. (2018). "The Size, Distribution, and Mobility of Landslides Caused by the 2015 Mw7.8 Gorkha Earthquake, Nepal". In: *Geomorphology* 301, pp. 121–138. ISSN: 0169555X. DOI: 10.1016/j.geomorph.2017.01.030.

Roering, J. J. (Sept. 2008). "How Well Can Hillslope Evolution Models "Explain" Topography? Simulating Soil Transport and Production with High-Resolution Topographic Data". In: *GSA Bulletin* 120.9-10, pp. 1248–1262. ISSN: 0016-7606. DOI: 10.1130/B26283.1. (Visited on 11/05/2025).

Romeo, R. (Dec. 2000). "Seismically Induced Landslide Displacements: A Predictive Model". In: *Engineering Geology* 58.3, pp. 337–351. ISSN: 0013-7952. DOI: 10.1016/S0013-7952(00)00042-9. (Visited on 04/23/2024).

Rubner, Y., C. Tomasi, and L. J. Guibas (Nov. 2000). "The Earth Mover's Distance as a Metric for Image Retrieval". In: *International Journal of Computer Vision* 40.2, pp. 99–121. ISSN: 0920-5691, 1573-1405. DOI: 10.1023/A:1026543900054. (Visited on 10/13/2025).

Saulnier, G.-M., K. Beven, and C. Obled (Dec. 1997). "Including Spatially Variable Effective Soil Depths in TOPMODEL". In: *Journal of Hydrology* 202.1, pp. 158–172. ISSN: 0022-1694. DOI: 10.1016/S0022-1694(97)00059-0. (Visited on 11/03/2025).

Segoni, S., G. Rossi, and F. Catani (Mar. 2012). "Improving Basin Scale Shallow Landslide Modelling Using Reliable Soil Thickness Maps". In: *Natural Hazards* 61.1, pp. 85–101. ISSN: 1573-0840. DOI: 10.1007/s11069-011-9770-3. (Visited on 11/03/2025).

Strauch, R. et al. (Feb. 2018). "A Hydroclimatological Approach to Predicting Regional Landslide Probability Using Landlab". In: *Earth Surface Dynamics* 6.1, pp. 49–75. ISSN: 2196-632X. DOI: 10.5194/esurf-6-49-2018. (Visited on 04/08/2024).

Tang, R. et al. (2025). "PyQuake3D: A Python Tool for 3-D Earthquake Sequence Simulations of Seismic and Aseismic Slip". In: *Journal of Geophysical Research: Machine Learning and Computation* 2.4, e2025JH000871. ISSN: 2993-5210. DOI: 10.1029/2025JH000871. (Visited on 10/31/2025).

Tanyaş, H. et al. (2017). "Presentation and Analysis of a Worldwide Database of Earthquake-Induced Landslide Inventories". In: *Journal of Geophysical Research: Earth Surface* 122.10, pp. 1991–2015. ISSN: 2169-9011. DOI: 10.1002/2017JF004236. (Visited on 03/27/2025).

Tsai, C.-C. and C.-H. Lin (Oct. 2018). "Prediction of Earthquake-Induced Slope Displacements Considering 2D Topographic Amplification and Flexible Sliding Mass". In: *Soil Dynamics and Earthquake Engineering* 113, pp. 25–34. ISSN: 0267-7261. DOI: 10.1016/j.soildyn.2018.05.022. (Visited on 11/11/2025).

Ulrich, T. et al. (Mar. 2019). "Dynamic Viability of the 2016 Mw 7.8 Kaikōura Earthquake Cascade on Weak Crustal Faults". In: *Nature Communications* 10.1, p. 1213. ISSN: 2041-1723. DOI: 10.1038/s41467-019-09125-w. (Visited on 01/21/2025).

USGS (2015). *M 7.8 - 67 Km NNE of Bharatpur, Nepal*. https://earthquake.usgs.gov/earthquakes/eventpage/us20002926/exec (Visited on 11/05/2015).

Wang, J. et al. (June 2020). "Long-Term Patterns of Hillslope Erosion by Earthquake-Induced Landslides Shape Mountain Landscapes". In: *Science Advances* 6.23, eaaz6446. DOI: 10.1126/sciadv.aaz6446. (Visited on 11/06/2025).

Westen, C., E. A. Castellanos Abella, and S. Kuriakose (Dec. 2008). "Spatial Data for Landslide Susceptibility, Hazard, and Vulnerability Assessment: An Overview". In: *Engineering Geology* 102, pp. 112–131. DOI: 10.1016/j.enggeo.2008.03.010.

Wong, H. and K. Ho (2000). *Preliminary Quantitative Risk Assessment of Earthquake-Induced Landslides at Man-Made Slopes in Hong Kong*. Tech. rep. GEO Report No. 98. Hong Kong SAR: Civil Engineering Department: Geotechnical Engineering Office.